



Nanoscale

Hierarchical nanotwins in single-crystal-like Nickel with high strength and corrosion resistance produced via a hybrid technique

Journal:	<i>Nanoscale</i>
Manuscript ID	NR-COM-08-2019-007472.R1
Article Type:	Communication
Date Submitted by the Author:	27-Nov-2019
Complete List of Authors:	<p>Li, Qiang; Purdue University System Xue, Sichuang; Purdue University System Price, Patrick ; Sandia National Laboratories Sun, Xing; Purdue University System, Materials Engineering Ding, Jie; Purdue University Shang, Zhongxia; Purdue University, School of Materials Engineering Fan, Zhe; Oak Ridge National Laboratory Wang, Han; Purdue University Zhang, Yifan; Purdue University Chen, Youxing ; Los Alamos National Laboratory, MPA-CINT Wang, Haiyan; Purdue University System, MSE; Neil Armstrong Engineering Building Hattar, Khalid; Sandia National Laboratories Zhang, Xinghang; Purdue University System, Materials Engineering</p>

SCHOLARONE™
Manuscripts

Hierarchical nanotwins in single-crystal-like Nickel with high strength and corrosion resistance produced *via* a hybrid technique

Qiang Li^a, Sichuang Xue^a, Patrick Price^b, Xing Sun^a, Jie Ding^a, Zhongxia Shang^a, Zhe Fan^c, Han Wang^a, Yifan Zhang^a, Youxing Chen^d, Haiyan Wang^{a,e}, Khalid Hattar^b and Xinghang Zhang^{a,}*

^a School of Materials Engineering, Purdue University, West Lafayette, IN 47907, United States

^b Sandia National Laboratories, Albuquerque, NM 87185, United States

^c Materials Science and Technology Division, Oak Ridge National Laboratory, Oak Ridge, TN 37831, United States

^d Department of Mechanical Engineering and Engineering Science, University of North Carolina at Charlotte, Charlotte, NC 28223, United States

^e School of Electrical and Computer Engineering, Purdue University, West Lafayette, IN 47907, United States

* Corresponding author: xzhang98@purdue.edu

KEYWORDS: Hierarchical nanotwins; Hybrid technique; Nickel; Mechanical property; Corrosion

Abstract

High-density growth nanotwins enable high-strength and good ductility in metallic materials. However, twinning propensity is greatly reduced in metals with high stacking fault energy. Here we adopted a hybrid technique coupled with template-directed heteroepitaxial growth method to fabricate single-crystal-like, nanotwinned (nt) Ni with anomalously high-density nanoscale twins. The nt Ni primarily contains hierarchical twin structures that consist of coherent and incoherent twin boundary (CTB and ITB) segments with few conventional grain boundaries. *In situ* compression studies show the nt Ni has a high flow strength of ~ 2 GPa and good deformability. Moreover, the nt Ni offers superb corrosion behavior due to the unique twin structure in comparison to coarse grained and nanocrystalline counterparts. The hybrid technique opens the door for the fabrication of a wide variety of single-crystal-like nt metals with unique mechanical and chemical properties.

1. Introduction

Nanotwinned (nt) metals have shown a desirable combination of mechanical and physical properties, such as high strength with preserved ductility, superb creep and thermal stabilities, low intrinsic electric resistivity and high resistance to localized corrosion¹⁻⁴. These nt metals have highly oriented twin lamellae terminated by grain boundaries (GBs) in equiaxed or columnar grains. Twin boundaries (TBs) can impede the glide of dislocations to harden materials⁵⁻⁹, and TBs also serve as sites for dislocation storage or migrate by means of successive motions of partial dislocations to accommodate plastic deformations, as evidenced empirically and computationally¹⁰⁻¹⁴. Nt metals have potential applications as structural materials and in three-dimensional integrated circuits and micro/nanoelectromechanical systems¹⁵⁻¹⁷.

Most of nt metals fabricated to date have low-to-intermediate stacking fault energy (SFE), *e.g.* Ag (16 mJ/m²), Au (32 mJ/m²), Cu (45 mJ/m²) and 330 austenitic stainless steel (10-20 mJ/ m²)^{5, 7, 15, 18-23}. Their twinnability is attributed to comparably small difference between perfect and twin nucleus radius and low unstable twinning (γ_{ut}) to unstable SFE (γ_{usf}) ratio^{19-21, 24}. Extensive efforts have been made to examine the properties of nt Cu, and major interests in studies of nt Cu originate from the TB-enabled high strength and good ductility as well as its low electric resistivity at ambient conditions. For instance, electrodeposited polycrystalline nt Cu with equiaxed grains and gradient columnar nt Cu have a maximum yield strength of ~ 900 MPa and an ultimate tensile strength of ~ 520 MPa, respectively^{6, 14}; moreover, sputtered epitaxial nt Cu with columnar grains has a hardness exceeding 3 GPa⁷. However, GBs in equiaxed or columnar nt metals are stress concentrators and sites that often initiate void formation, leading to reduced ductility^{16, 25-27}. Moreover, TB-GB junctions often act as dislocation nucleation sources to decrease strength²⁸. Nt metals manifest improved corrosion behavior because TBs with low boundary free energy alleviate intergranular corrosion^{4, 29, 30}. Recent studies show that nanotwins in equiaxed or columnar grains assist the formation of thin and continuous passive layers and thus enhance corrosion resistance³⁰⁻³². It is worth noting that high-density GBs in nc metals could facilitate fast diffusion for formation of protective passive film, but may also serve as active sites for preferential corrosive attack^{29, 33}. Influence of stand-alone TBs on deformation behaviors and corrosion behaviors of nt metals is hardly investigated as TBs often coexist with GBs³⁴. Although GB-free nt materials have been occasionally achieved in high-aspect-ratio nanostructures, such as nanowires and nanopillar^{23, 35-37}, it is in general difficult to fabricate GB free nt metals.

In metals with high SFE, it is difficult to introduce high-density growth twins due to the high energy penalty. For Ni with a high SFE of 120-130 mJ/m² ³⁸, deformation twins were created either in nanocrystals ^{2, 39, 40}, under high strain rate deformation ⁴¹, or through alloying tactics to reduce SFE ⁴²⁻⁴⁴. Annealing twins were developed in pulsed-laser deposited Ni thin films ^{45, 46}. Recent studies show that nanoscale growth twins can be introduced in Ni *via* co-sputtering of Ni with Mo and W solutes ¹⁶. Furthermore, electrodeposition can induce growth twins in polycrystalline Ni with equiaxed grains ^{47, 48}.

Here, we report a hybrid technique to fabricate single-crystal-like nt Ni that possesses primarily coherent twin boundaries (CTBs) and incoherent TBs (ITBs) with few GBs. Sputtering offers nt Cu template for heteroepitaxial growth of nt Ni *via* electrodeposition. The construction of metallic films by TBs with few conventional GBs is reported for the first time, to the best of our knowledge. Our studies show that the synergistic effect from template and electrochemical additives can effectively control the microstructure of nt Ni *via* the hybrid technique. The single-crystal-like nt Ni has high strength, significant deformability and excellent corrosion response. We envision that this study may open opportunities to synthesize a variety of high-strength, deformable nt metals with high SFEs.

2. Results

2.1 Fabricate single-crystal-like nt Ni via hybrid technique

To prepare twinned Ni, a hybrid technique consisting of sputtering and electrodeposition methods is used, as illustrated in Figure 1a. 1- μ m thick nt Cu (111) films were first sputter-deposited onto Si (110) substrates as templates (referred to as Cu (111) template hereafter) (Figure 1a and 1b) ^{7, 49, 50}. The automated crystal orientation map (ACOM) in Figure 1c reveals

that sputtered Ni on Cu (111) template has twins (referred to as s-nt Ni), also supported by the pole figure observation, but the twin spacings are fairly large. Next, we turn our attention to a hybrid fabrication technique wherein Ni is electrodeposited in aqueous electrolyte onto sputtered Cu templates (see the details in experiment procedures). Interestingly, the ACOM in Figure 1d shows that the electrodeposited Ni contains high-density nanotwins (referred as e-nt Ni hereafter). The matrices and twins are separated by wavy TBs and no conventional and columnar GBs are observed. Such a microstructure is different from most of the previously reported nt metals that show TBs are terminated at well-defined columnar or equiaxed GBs^{5, 7, 15, 51}. A majority of the TBs appear curved, consisting of a complex blend of $\Sigma 3\{111\}$ CTB and $\Sigma 3\{112\}$ ITB segments. Selected area diffraction (SAD) pattern reveals that e-nt Ni was heteroepitaxially grown on Cu (111) in Figure S1. The e-nt Ni is composed of traces of nonmetallic impurity.

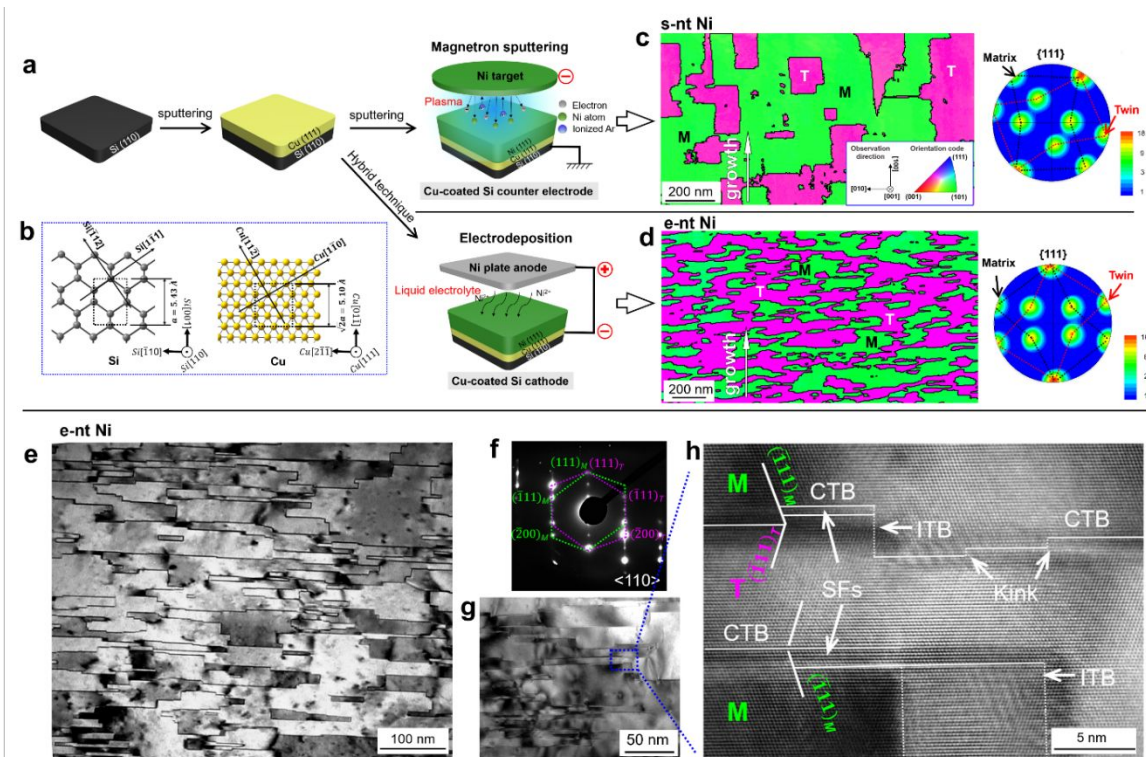


Figure 1. Fabrication and microstructure of single-crystal-like nanotwinned (nt) Ni *via* a hybrid technique. (a) Methodological approaches to heteroepitaxially grow nt Ni on Cu (111) coated Si substrates using either monolithic magnetron sputtering technique or a hybrid technique. (b) Crystallographic relationship between Cu (111) and Si (110) substrate. (c) An automated crystal orientation map (ACOM) of sputtered nt Ni (s-nt Ni) with coarse twin structures. The pole figure indicates textured and twinned structure. (d) ACOM of electrodeposited nt Ni (e-nt Ni) *via* a hybrid technique. Twin boundaries (TBs) are marked in black lines. Few ambiguities and conventional GBs are spotted and mostly all boundaries are determined as $\Sigma 3$ TBs. They exhibit wavy structure. The pole figure indicates textured and twinned structure. (e) Low-magnification Cross-sectional TEM (XTEM) micrograph showing high-density stepped nanotwins with long and irregular step morphology. (f) Corresponding SAD pattern showing a typical twin diffraction pattern. (g) Intermediate magnification TEM micrograph highlighting the stepped TBs composed of CTB and ITB segments. (h) HRTEM micrograph showing that the CTBs are decorated by kinks and stacking faults (SFs), and ITBs sometimes have diffuse character with a width of ~ 10 nm. Note: *M* and *T* stand for matrix and twin, respectively.

2.2 Attributes of twin structures

Cross-section transmission electron microscopy (XTEM) micrograph in Figure 1e confirms that the TBs in e-nt Ni have hierarchical structure. A majority of twins have ultra-long

CTBs interrupted by multiple vertical ‘stairs’ (ITB steps); and there are numerous secondary finer nanotwins distributed randomly within the matrix. No clear columnar GBs exist. The SAD pattern in Figure 1f shows a typical twin diffraction pattern. The stepped nanotwins are shown in magnified HRTEM micrograph in Figure 1g and 1h. HRTEM image also shows that CTBs are frequently decorated by planar SFs and kink-like ITB steps with 1-2 nm in height. Intrinsic GB dislocations that result from small angular deviation from orientation of coincident site lattice (CSL) boundaries could also induce faulted CTBs⁵². Diffuse ITB segments (several to a dozen nm in width) are also observed, and are often referred to as 9R phase in literature^{12, 53-56}. The nt Cu templates have a columnar grain size of ~ 120 nm, and the boundaries have not noticeably stretched across interface, except for introduction of threading dislocations into Ni layer. It is worth emphasizing that the electrochemical additive and template are vital for the formation of the unique hierarchical twin structure.

2.3 Microstructure and texture of different Ni

In monolithic sputtering technique, s-nt Ni films were sputtered on Cu (111) template. X-ray {111} pole figure in Figure 2a1 shows 6 equally bright spots in a hexagonal pattern at a Chi angle of $\sim 70.5^\circ$, indicating that the sputtered Ni has strong (111) texture and twin variants (Figure S2 and S3). S-nt Ni is composed of thick growth twins as evidenced from cross-section focused-ion-beam (XFIB) ion-channeling image (Figure 2a2), in agreement with ACOM studies in Figure 1c. Additionally, the epitaxial growth of the Ni film is supported by the plan-view TEM image with a SAD pattern taken along the Ni $\langle 111 \rangle$ zone axis shown in Figure 2a3. The long, vertical GBs are identified as ITBs (Figure S4) and abundant low angle GBs exist, which reduces the average columnar grain size to $\sim 30 \pm 15$ nm, whereas the average CTB spacing is $\sim 182 \pm 118$ nm.

The hybrid technique used different templates and electrochemical recipes. When a polycrystalline Cu template (grown on oxidized Si substrate) was adopted, the electrodeposited Ni possesses no obvious texture as shown in x-ray $\{111\}$ pole figure in Figure 1b1 (also in Figure S2 and S3). The polycrystalline Ni consists of nanocrystals somewhat elongated along the growth direction, evidenced by the XFIB and the plan-view TEM images in Figure 2b2 and 2b3. A few twins are captured. The average grain size is estimated to be 34 ± 16 nm. When Ni was electrodeposited on Cu (111) without organic additive (Sodium saccharin) in electrolyte solution, a (111) textured Ni film (referred to cg Ni hereafter) was obtained as shown in Figure 2c1. XFIB image in Figure 2c2 and TEM micrograph in Figure 2c3 show large grains with some inclined twins. XTEM observation shows an average grain size of ~ 454 nm, and TEM images (Figure S5a - S5f) show that the vertical and inclined defects are ITBs and stacking fault (SF) ribbons or inclined twins on $(\bar{1}11)$ glide planes. The inclined twin structure produces $(\bar{1}15)$ texture in twin variants, responsible for the diminishing (111) texture.

In comparison, through electrodeposition of Ni on Cu (111) with the addition of surfactant additive (referred as additive-assisted electrodeposition or AAEP hereafter) (see the details in experiment procedures), a single-crystal-like nt Ni, namely e-nt Ni, formed as shown in $\{111\}$ X-ray pole figure in Figure 2d1. Furthermore, XFIB image in Figure 2d2 displays fine and alternating contrast with wavy TBs in good coincidence with ACOM and TEM results in Figure 1. The plan-view TEM image taken at $\langle 111 \rangle$ zone axis substantiates the single-crystal-like characters (Figure 2d3). Both plan-view and cross section observations rarely show equiaxed or columnar GBs. The average CTB spacing is determined to be 22 ± 14 nm (Figure S6). During the electrochemical growth of twin structure in e-nt Ni, some protrusions were observed on free surface and the twinned regime shows smooth and flat character, unlike the surface roughness on

nc Ni and cg Ni (Figure S7). Detailed texture information can be found in Figure S2 and S3. It is noteworthy that the e-nt Ni has been produced on Cu (111) template under equivalent electrodeposition conditions as cg Ni, but the inclusion of additive drastically changes the twin geometry and enhances the twinning propensity. The aforementioned findings suggest that the additive-assisted electrodeposition and Cu (111) template have a synergistic effect on producing the e-nt Ni *via* this hybrid approach.

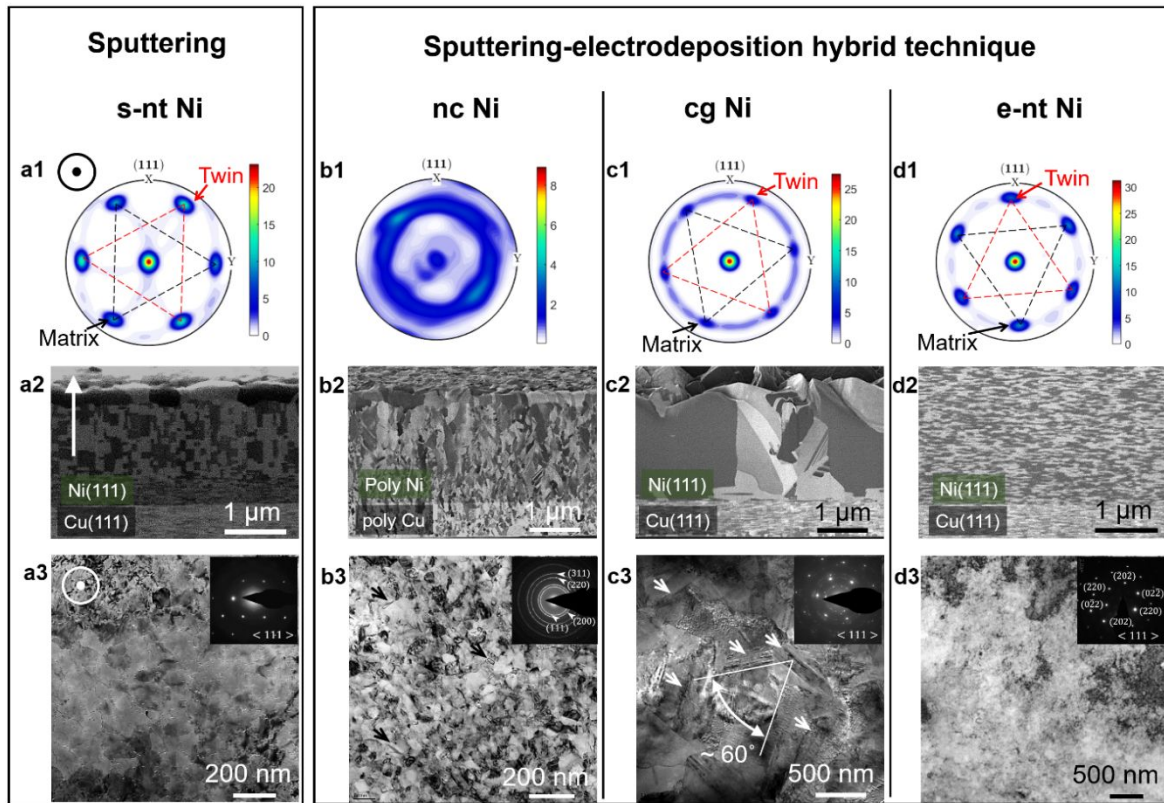


Figure 2. Tailoring microstructure of Ni synthesized by various conditions. (a1-a3) Sputtered nt Ni (s-nt Ni) on Cu (111) template. {111}; X-ray pole figure analysis in (a1) shows 6-fold symmetric spots arising from the matrix and twin variants. Cross-sectional focused-ion-beam ion channeling (XFIB) image in (a2) shows block-like twin structure with large twin spacing in Ni. Plan-view TEM micrograph in (a3) shows columnar grain boundaries. (b1-b3) Additive-assisted electrodeposition of nanocrystalline Ni (nc Ni) on sputtered polycrystalline Cu template. X-ray pole figure (b1) shows no sign of (111) texture in nc Ni. XFIB (b2) and plan-view TEM (b3) micrographs show the formation of nanocrystals. (c1-c3) Additive-free electrodeposition of coarse-grained (cg) Ni on sputtered nt Cu (111) template. X-ray pole figure in (c1) reveals the occurrence of twins. XFIB (c2) and plan-view TEM (c3) micrographs show inclined twin boundaries in cg Ni. (d1-d3) Additive-assisted electrodeposition of single-crystal-like nt Ni (e-nt Ni) on nt Cu (111) template. X-ray pole figure in (d1) shows the formation of high-density twins. XFIB image in (d2) displays the formation of extremely fine twins with no presence of columnar grain boundaries. Plan-view TEM image in (d3) and the inserted SAD pattern suggests single-crystal-like structure. Symbols in column I indicate the film growth direction.

2.4 *In situ* compression experiments

In situ compression experiments have been carried out on the four Ni specimens inside a scanning electron microscope (SEM). Figure 3a shows the engineering stress-strain curves for the cg Ni, nc Ni, s-nt Ni and e-nt Ni, and their corresponding SEM snapshots captured at different strains (Figure 3b-e). At 5 % strain, the flow stress of the e-nt Ni micropillars is ~ 2.1 GPa, followed by ~ 1.64 GPa of nc Ni, ~ 1.41 GPa of s-nt Ni and ~ 0.88 GPa of cg Ni. Two partial unloading curves were deliberately added at strains less than 5 % to inspect the alignment reliability. The deformed cg Ni micropillars showed slip bands, whereas e-nt Ni, s-nt Ni and nc Ni deformed in a more homogeneous manner without shear bands (Figure 3b-e). No serrations associated with dislocation bursts were observed in the stress-strain curves.

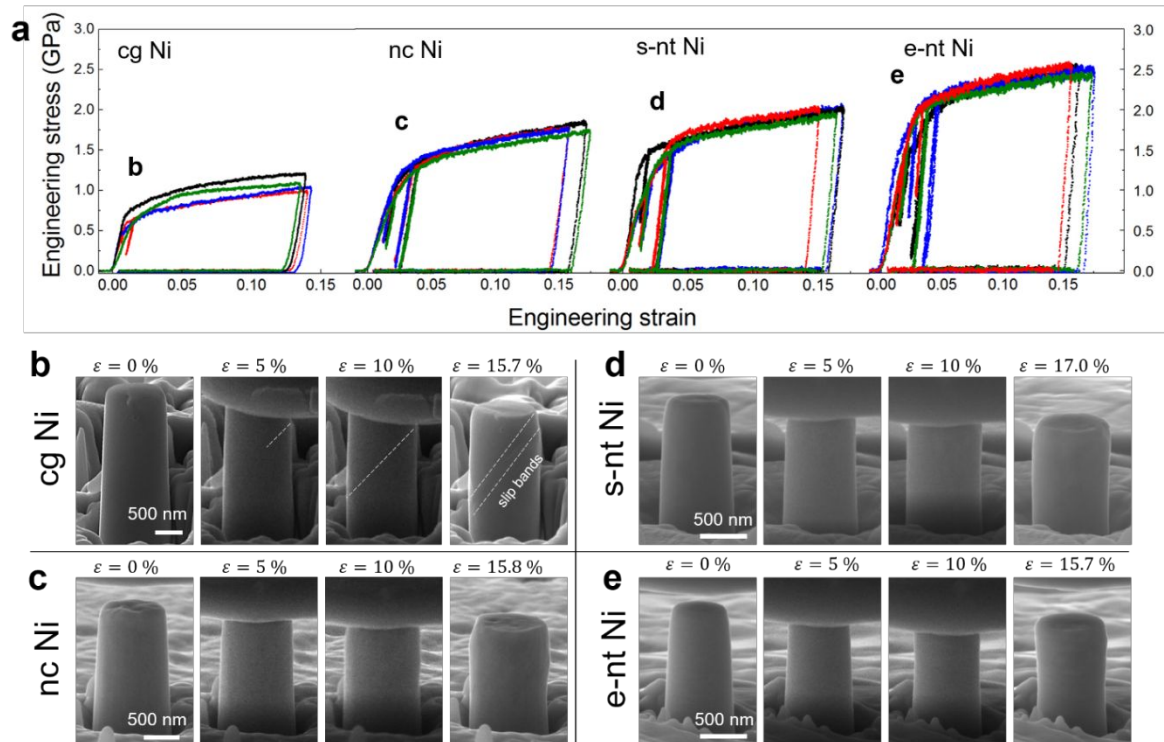


Figure 3. *In situ* compression experiments (inside a scanning electron microscope) on Ni samples prepared by various processes. (a) Engineering stress-strain curves of cg Ni, nc Ni, s-nt Ni and e-nt Ni show that e-nt Ni outperforms its counterparts. (b-e) Snapshots of deformed micropillars at different strain levels show the formation of shear off-sets in cg Ni; whereas no obvious localized deformation occurs in other samples. See supplementary movie S1-S4.

3. Discussion

3.1 Twin formation mechanism

The cross-sectional scanning TEM (STEM) image together with energy dispersive X-ray spectroscopy (EDS) map (Figure S1c) mark the notable Ni/Cu interface. Furthermore, the SAD patterns captured at Cu/Ni interface in e-nt Ni confirm the orientation relationship as Ni $[111]//\text{Cu } [111]//\text{Si } [110]$, and Ni $[1\bar{1}0]//\text{Cu } [1\bar{1}0]//\text{Si } [1\bar{1}1]$ ^{7, 57}. The epitaxial growth of Ni on Cu is based on their small lattice mismatch, $\sim 2.6\%$ ($a_{\text{Cu}} = 3.615 \text{ \AA}$; $a_{\text{Ni}} = 3.52 \text{ \AA}$). Epitaxial growth of nt Cu (111) in columnar grains on Si (110) substrate has been well documented^{7, 49, 50}.

Electrodeposition is a high-flux non-equilibrium growth technique, wherein strain energy and surface energy constantly compete. The electrodeposited Ni often develops (200) texture in equiaxed nc Ni ⁵⁸, in agreement with the texture in nc Ni in this study (shown in Figure S3b). The formation of (111) texture in s-nt Ni, cg-Ni and e-nt Ni is ascribed to the heteroepitaxial growth of Ni on Cu template.

The cg Ni also has a dominant (111) texture due to the usage of Cu (111) template, but contains inclined CTBs in coarse grains as shown in Figure S6f, resulting in formation of crystallites with ($\bar{1}15$). S-nt Ni films have long ITBs formed due to island impingement during grain coalescence and the CTB spacing is as large as 182 ± 118 nm because of its high SFE. TBs have been introduced into Ni across coherent layer interfaces in nanolayered Cu/Ni films ⁵⁷. From a theoretical perspective, it is expected that low SFEs, γ_{sf} , low temperature and high-flux deposition can enhance the twinning propensity ¹⁹. Randomly oriented twins were recently observed in sputtered and electrodeposited polycrystalline Ni ⁵⁹. Coarse twins have been introduced in Ni prepared by sputtering at -150 °C and at a high deposition rate of 125-300 Å/s ⁶⁰.

The current study shows that both template and electrochemical recipes play crucial roles on the formation of distinctive twin structure in e-nt Ni. While the Cu template promotes the (111) texture in Ni, the additive in aqueous solution may refine the twins by preventing the successive growth of twinned crystals. This proposition will be discussed further.

Typically, the microstructure of electrodeposited metals on single-crystal substrate may undergo a sequential transition from nanometric epitaxial zone to polycrystals and 3D clusters during growth ⁶¹. The (111) textured cg Ni appears to follow such a three-dimensional (3D)

growth mode, and ITBs arise from impingement of large islands^{21, 62}. Note that no additives were applied during the growth of cg Ni. In contrast, the e-nt Ni deposited with the assistance of additives contains high-density hierarchical nanotwins, for which a swapped growth mechanism may be responsible. Organic additives used in electroplating are known as inhibitors and prone to adsorb on cathode surface to rise overpotential^{63, 64}. Therefore, Ni²⁺-containing intermediates are expected to be obstructed in motions and surrounded by negatively charged benzene rings and thus promote nucleation and reduce island radius^{65, 66}. The adsorbate usually promotes a 3D cluster growth mode upon polycrystalline growth. However, Cu template-stimulated (111) texture solely renders the growth of two types of nuclei, namely matrix nuclei with a 60 ° in-plane rotation (along <111> axis) as to the twin nuclei in terms of crystallographic orientation⁶⁷. The nuclei as individual growth centers laterally grow at the expense of the surrounding crystallites with identical orientation. Then, they laterally merge, impinge by annihilating free surface and forming ITBs and eventually evolve into a continuous thin layer. On the contrary, cg Ni with no aid from additive is inevitably subjected to coalescence and 3D cluster growth (Volmer-Weber mode). Additive aids in lateral growth, which was verified in electrodeposited Cu⁶⁸. The additives in the growth of single-crystal-like Ni favor a transition from a 3D cluster growth (Volmer-Weber mode) to a flat quasi-2D layer-to-layer growth mode⁶². Consequently, the additives promote a quasi-2D growth of fine Ni (111) twins on the Cu (111) template, without experiencing island coalescence. We hypothesize that the CTB segment formation and ITB termination may be attributed to disturbance of surfactant molecules wrapping nuclei and/or energy minimization that prevents formation of long ITB segments. The formation of long ITBs in Ni is energetically difficult due to its high ITB energy, ~ 1,469 mJ/m², whereas CTB energy in Ni is merely 63 mJ/m²⁶⁹.

3.2 Strengthening and plasticity

3.2.1. Strengthening mechanisms

Nt metals with equiaxed or columnar grains have abundant GBs and TBs, which both impact the mechanical behaviors. To better understand the influence of TBs on the mechanical behaviors, the flow stresses of Ni specimens measured in this study are compared to prior studies in a Hall-Petch plot in Figure S8, where the data on nc or nt Ni were collected from either compressive or tensile tests. The linear fit of literature data gives a slope of $\sim 6.1 \pm 0.3 \text{ GPa} \bullet \sqrt{nm}$, comparable to the empirical value of $\sim 5.7 \text{ GPa} \bullet \sqrt{nm}$ for polycrystalline Ni reported previously⁷⁰⁻⁷². In some studies, inverse Hall-Petch relation has been observed in nc Ni when grain size is $\sim 20\text{-}50 \text{ nm}$ ⁷². However, the e-nt Ni (with an average twin spacing of 22 nm) does not show softening and reaches a flow stress of $\sim 2.1 \text{ GPa}$ at 5% strain, exceeding the prediction from the Hall-Petch slope derived from nc Ni.

The Hall-Petch strengthening cannot solely account for the high strength of e-nt Ni, which requires further discussion. First, CTBs are effective barriers for dislocation transmission. The compressive direction promotes dislocations with both slip plane and slip direction inclined to CTBs, causing effective blockage of dislocation transmission^{10, 73, 74}. Second, we notice that the e-nt Ni has a wide distribution of twin spacing, and nearly 35% of twins have a thickness of 10 nm or less (Fig. S7d). Hence, the high yield strength of e-nt Ni may be closely tied to the dislocations in partial emission and confined layer slip (CLS) mechanisms within these small

twins. Details on the calculated strength based on CLS mechanism is shown in supplementary information and the results shown in Fig. S8 appear to capture the size dependent strengthening in nt-Ni well. Third, SFs near CTBs might enhance the barrier resistance of TBs to transmission of dislocations comparing to clean CTBs. There are recent studies showing that He radiation induced SFs at CTBs in Cu can lead to ultra-high strength in nt Cu ⁷⁵. Other factors might also contribute to strengthening, such as interstitial solid-solution strengthening and (111) texture that leads to a 3.67 of Taylor factor versus 3.06 in polycrystals.

3.2.2. Detwinning

Post-mortem TEM analyses were performed on deformed e-nt Ni along $\langle 110 \rangle$ direction. Figure 4a shows that a deformation up to $\sim 16\%$ strain changes the twin morphology prominently. The inset SAD shows stretched diffraction spots that signal lattice distortion. TEM image suggests that a large number of vertical ITB steps were removed, suggesting the occurrence of detwinning. But the detwinning we observed in e-nt Ni is quite different from what has been reported previously in nt Cu, where detwinning leads to appreciable softening and eventually highly localized deformation ⁷⁵. The detwinning in the current study leads to long, comparably smooth CTBs, and the thickness of twins increases moderately to ~ 37 nm. SAD patterns captured throughout the deformed pillar in Figure S9 illustrate that the lattice distortion/rotation occurs mainly in the upper deformed portion of the pillar. A corresponding ACOM micrograph and the pole figure image shown in Fig. 4b agrees with TEM observation of lattice distortion. For example, two crosses marked on the ACOM (Fig. 4b) within one long matrix crystal represent $(\bar{3}1\bar{5})$ and $(\bar{7}3\bar{8})$, with a $\sim 11^\circ$ relative rotation. Figure 4c implies that the deformation created a ~ 25 nm tall ITB segment with no steps, but the (111) planes within matrix and twin regimes have a $\sim 15^\circ$ relative misorientation. The deformation-induced bending

of the (111) planes may develop a resolved shear stress on the Shockley partials⁷⁶. The ITB steps containing partials could migrate through collective glide of partial dislocations, leading to detwinning^{12, 13, 77}. HRTEM micrographs in Figure 4d-e reveal numerous steps on the CTBs. Furthermore, on the ($\bar{1}11$) planes inclined to the CTBs, Shockley partials (some of which are identified as $90^\circ 1/6\langle 112 \rangle$ partials) were frequently observed. Many of the partials appear to be blocked by CTBs. Frank partials are frequently associated with the generation of steps on CTBs. Prior molecular dynamic (MD) simulations and *in situ* TEM nanoindentation studies show that dislocation multiplications leave cumulative Franks and twinning dislocations on CTBs during transmission or through a dislocation multiplication mechanism^{78, 79}. A study on dynamic compression-induced curved CTBs revealed that the curvature may derive from ITB steps generated during dislocation-CTB interactions⁸⁰.

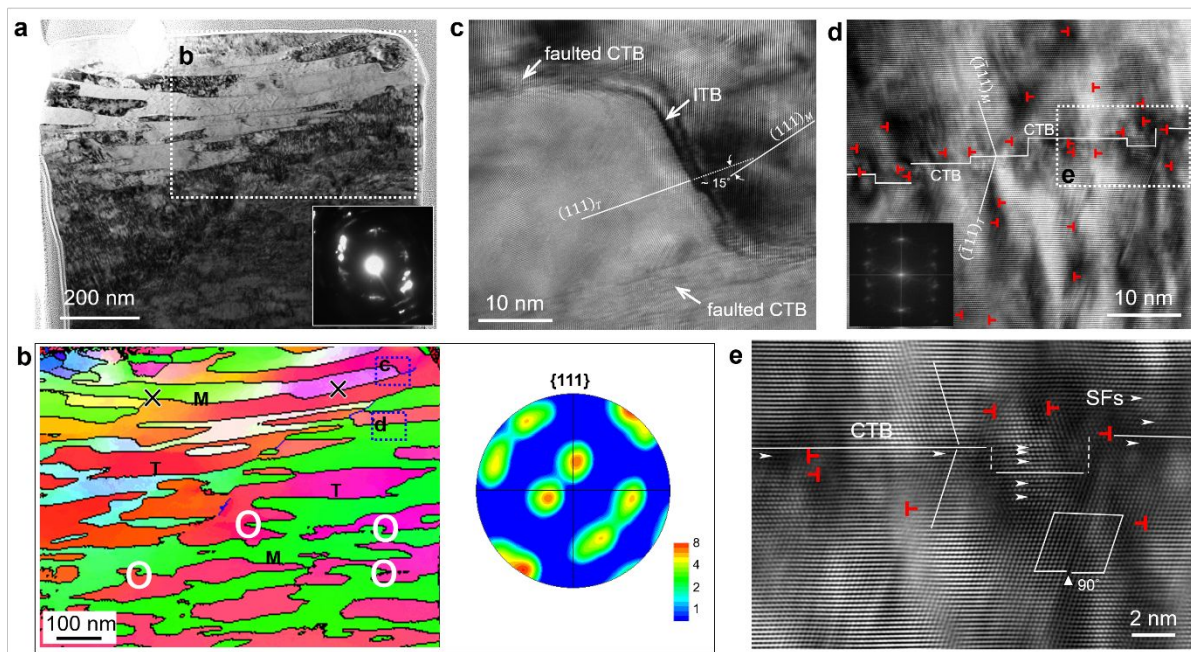


Figure 4. Post-mortem XTEM/ACOM micrographs of the single-crystal-like e-nt Ni micropillar deformed up to ~16 % strain. (a) Low magnification bright-field TEM micrograph and corresponding SAD pattern show {111} lattice plane rotation and curved CTBs in deformed twin structures. (b) Corresponding ACOM image shows long CTBs, and the removal of irregular ITB steps in the deformed pillar top region, whereas stepped irregular twins with CTB and ITB

segments remain in the lower portion of less deformed region. The pole figure indicates lattice plane rotation. (c) TEM image shows curved TBs after deformation, and the rotation of (111) planes in matrix and twins. (d) TEM image shows the formation of steps along CTBs and the dislocation activities. Abundant Frank partials form adjacent to CTBs. (e) High-resolution TEM image shows 90° Shockley partials are blocked by TBs containing SFs and steps.

3.2.3. Strain hardening of nt Ni

It is also worth mentioning that the e-nt Ni pillars show more homogeneous deformation, in comparison with highly localized deformation signified by pillar dilation on the top in nanolaminate systems and conventional nt metals with GBs^{75, 81-83}, indicative of plastic instability. *In situ* micropillar compression studies shows that e-nt Ni has high strength and extensive deformability. Micropillars of e-nt Ni with different diameters spanning from 0.7 to 3 μm have been deformed (Figure S10) and it shows no apparent extrinsic size effect, different from single crystals⁸⁴⁻⁸⁸ and nanocrystalline materials⁸⁹. The underlying principle for the absence of extrinsic size effect requires future studies. Various Ni samples react differently to deformation upon *in situ* compression, and therefore we developed a methodology detailed in supplementary information to interpret true stress-strain curves by taking spontaneous change of indenter-pillar contact area into account. Despite softening from detwinning, the e-nt Ni exhibits an overall strain hardening behavior, evidenced by a ~ 2.2 GPa of hardening rate between 5 to 12 % strain (Figure S11), in contrast to the localized deformation in nt Cu with orthogonal twins in columnar structure, indicative of strain softening^{75, 82}. Other Ni samples show higher hardening rates due to larger feature size that permits dislocation multiplication. The superb deformability of e-nt Ni is tied to the unique twin structure. Although the e-nt Ni has an average twin spacing of ~ 22 nm, twins can be as fine as a few nanometers and as thick as ~ 100 nm. When dislocations are nucleated and pile up against TBs, work hardening arises from the resistance of

TBs to the transmission of dislocations and multiplication. Due to the wide distribution of twin thickness, dislocation and TB dictated deformation mechanisms are size dependent, as illustrated in Figure S12. With decreasing twin spacing, the deformation mechanisms may evolve from pile-up of perfect dislocations, to confined layer slip (CLS, similar to Orowan-type dislocation bowing) and then to partial dislocation emission^{10, 16, 26, 90}. The fine and large nanotwins would act as dislocation barriers and plasticity carriers simultaneously. When dislocations propagate through narrow or wide twin channels *via* CLS mechanism, a variable (high or low) stress is necessary to push dislocations. Consequently, repetitive strain hardening and softening might also facilitate plasticity in e-nt Ni. The unique hierarchical twin structure hence permits both ultrahigh strength and superb plasticity.

3.3 Corrosion behavior

Figure 5 shows the comparison of the potentiodynamic polarization curves amongst various Ni specimens tested in artificial seawater, *i.e.* 3.5 wt. % NaCl solution. Relevant corrosive parameters that derive from analyses of polarization curves are summarized in Table S3. It shows that e-nt Ni delivers a corrosion potential of $E_{corr} = -166$ mV, appreciably higher than the ones of bulk-cg Ni, nc Ni and s-nt Ni, meanwhile e-nt Ni exhibits the low corrosion current density ($i_{corr} = 6.91 \times 10^{-8}$ A/cm²). Through Stern-Geary equation (see supplementary information)⁹¹, polarization resistance (R_p), inversely related to the corrosion rate, is deduced to determine the resistance of various Ni specimens against corrosive attack. Table S3 clearly shows that the e-nt Ni prepared by hybrid technique has the highest polarization resistance of 516 k Ω .

It is interesting to note that the s-nt Ni does not exhibit promising corrosion resistance. The polarization curve hints the lack of passivation of s-nt Ni. The long ITBs in s-nt Ni may lead to uninterrupted invasion of corrosion into films and the residual stress and nanovoids introduced during sputtering could potentially deteriorate the corrosion pit resistance. Moreover, bulk-cg Ni with $\sim 60 \mu\text{m}$ grain size exhibits marginally more negative potential $E_{corr} = -200 \text{ mV}$ than $E_{corr} = -192 \text{ mV}$ of nc Ni, but apparently lower $i_{corr} = 1.59 \times 10^{-7} \text{ A/cm}^2$ than $i_{corr} = 1.24 \times 10^{-6} \text{ A/cm}^2$ of nc Ni. Prior studies express that the lower i_{corr} of cg Ni is ascribed to small amount of active sites at GBs^{29, 92}. High-density GBs in nc metals assist fast diffusion and formation of the passive layer but, at the same time, are active sites for preferential corrosion and hence no board consensus on superiority between cg and nc metals has been reached^{29, 33}. Though impurities render insignificant hardening in Ni specimens prepared *via* hybrid technique, involvement of additives comparably increases the sulfur concentration and it was reported that sulfur in nc Ni increases current density and delays passivation because sulfur diffuses and forms non-protective sulphide film where sulfur competes with OH^- groups for adsorption sites (OH^- is a precursor for the formation of passive film)⁹³. This might contribute to the highest $i_{corr} = 1.24 \times 10^{-6} \text{ A/cm}^2$ of nc Ni.

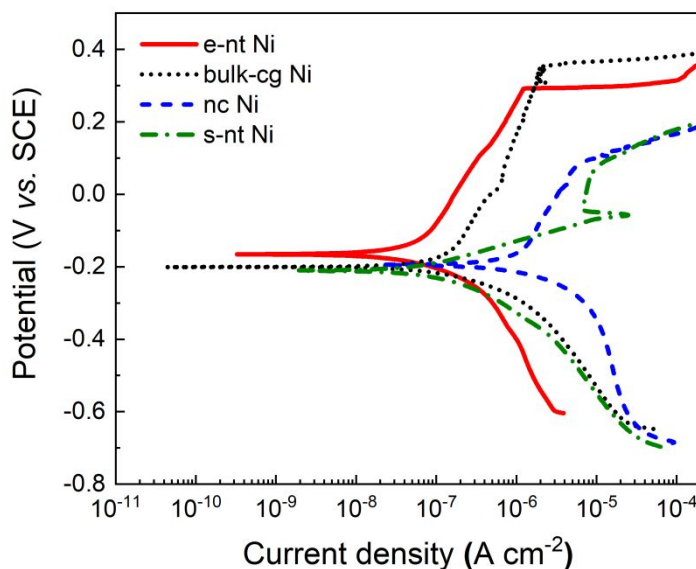


Figure 5. Potentiodynamic polarization curves of bulk-cg Ni, nc Ni, s-nt Ni and e-nt Ni in artificial seawater. The e-nt Ni shows most positive corrosion potential and lowest corrosion current density amongst various Ni specimens.

From the perspective of GB engineering described in the coincidence site lattice (CLS), low Σ boundaries generally have higher resistance to intergranular corrosion^{94, 95}. For instance, an improved corrosion behavior was observed in Cu with horizontal twins in columnar grains where corrosion was affected by columnar GBs composed of both high-angle and low-angle GB segments³²; nanotwins in polycrystalline Ni could influence diffusion of point defects and generate a thinner but less defective passive layer³⁰.

Though factors, such as texture, trace impurity, irregular surface protrusion *etc.*, could influence corrosion behavior, the unique hierarchical twin network predominantly accounts for the superb corrosion response of e-nt Ni when comparing to other counterparts. Excess vertical ITB segments that arrive at free surface are expected to be susceptible to corrosion and

meanwhile facilitate the fast diffusion for the formation of passive layer due to their high boundary energy. It is hypothesized that the propagation of corrosive path along short ITB segments would terminate in single-crystal-like matrix and be arrested by the ITB-CTB junctions. The construction of hierarchical twin structure in single-crystal-like Ni thus may suppresses the localized intergranular corrosion; in addition, Ni ions could diffuse out of the short but dense ITB segments to rapidly form passive layer. These give rise to a low corrosion rate in the e-nt Ni.

Conclusions

We applied a hybrid technique that integrates sputtering and additive-assisted electrodeposition to heteroepitaxially grow a single-crystal-like nanotwinned Ni with an average twin spacing of 22 ± 14 nm. The hierarchical twin structure contains a complex blend of coherent twin boundaries and incoherent twin boundaries with few grain boundaries. We showed that the template and carefully conceived electrochemical solution concurrently change twin propensity and twin structure. *In situ* compression studies revealed that the electrodeposited nt Ni delivered a maximum flow stress exceeding 2 GPa, and extensive deformability due to the unique twin structures. Moreover, the nt Ni has the highest corrosion resistance in comparison with other Ni with different microstructures. This study offers opportunities to fabricating high strength, deformable and corrosion resistant nanotwinned metals with high stacking fault energies for various applications.

Acknowledgements

We acknowledge financial support from DoE-BES under grant no. DE-SC0016337. This work was performed, in part, at the Center for Integrated Nanotechnologies, an Office of Science

User Facility operated for the U.S. Department of Energy (DOE) Office of Science. Sandia National Laboratories is a multimission laboratory managed and operated by National Technology & Engineering Solutions of Sandia, LLC, a wholly owned subsidiary of Honeywell International, Inc., for the U.S. DOE's National Nuclear Security Administration under contract DE-NA-0003525. The views expressed in the article do not necessarily represent the views of the U.S. DOE or the United States Government. Accesses to the Microscopy facilities at Purdue University are acknowledged.

Conflicts of interest

There are no conflicts to declare

Notes and References

1. I. J. Beyerlein, X. H. Zhang and A. Misra, *Annu Rev Mater Res*, 2014, **44**, 329-363.
2. Y. T. Zhu, X. Z. Liao and X. L. Wu, *Prog Mater Sci*, 2012, **57**, 1-62.
3. I. A. Ovid'ko, R. Z. Valiev and Y. T. Zhu, *Prog Mater Sci*, 2018, **94**, 462-540.
4. L. Y. Qin, J. S. Lian and Q. Jiang, *T Nonferr Metal Soc*, 2010, **20**, 82-89.
5. L. Lu, Y. F. Shen, X. H. Chen, L. H. Qian and K. Lu, *Science*, 2004, **304**, 422-426.
6. L. Lu, X. Chen, X. Huang and K. Lu, *Science*, 2009, **323**, 607-610.
7. O. Anderoglu, A. Misra, H. Wang, F. Ronning, M. F. Hundley and X. Zhang, *Appl Phys Lett*, 2008, **93**.
8. D. Bufford, Y. Liu, J. Wang, H. Wang and X. Zhang, *Nat Commun*, 2014, **5**.
9. H. F. Zhou, X. Y. Li, S. X. Qu, W. Yang and H. J. Gao, *Nano Lett*, 2014, **14**, 5075-5080.
10. Z. S. You, X. Y. Li, L. J. Gui, Q. H. Lu, T. Zhu, H. J. Gao and L. Lu, *Acta Mater*, 2013, **61**, 217-227.
11. Y. M. Wang, F. Sansoz, T. LaGrange, R. T. Ott, J. Marian, T. W. Barbee and A. V. Hamza, *Nat Mater*, 2013, **12**, 697-702.
12. J. Wang, N. Li, O. Anderoglu, X. Zhang, A. Misra, J. Y. Huang and J. P. Hirth, *Acta Mater*, 2010, **58**, 2262-2270.
13. N. Li, J. Wang, J. Y. Huang, A. Misra and X. Zhang, *Scripta Mater*, 2011, **64**, 149-152.
14. Z. Cheng, H. F. Zhou, Q. H. Lu, H. J. Gao and L. Lu, *Science*, 2018, **362**, 559.
15. H. Y. Hsiao, C. M. Liu, H. W. Lin, T. C. Liu, C. L. Lu, Y. S. Huang, C. Chen and K. N. Tu, *Science*, 2012, **336**, 1007-1010.
16. G. D. Sim, J. A. Krogstad, K. M. Reddy, K. Y. Xie, G. M. Valentino, T. P. Weihs and K. J. Hemker, *Sci Adv*, 2017, **3**.
17. C. L. Lu, H. W. Lin, C. M. Liu, Y. S. Huang, T. L. Lu, T. C. Liu, H. Y. Hsiao, C. Chen, J. C. Kuo and K. N. Tu, *Npg Asia Mater*, 2014, **6**.
18. D. Bufford, H. Wang and X. Zhang, *Acta Mater*, 2011, **59**, 93-101.

19. X. Zhang, A. Misra, H. Wang, T. D. Shen, M. Nastasi, T. E. Mitchell, J. P. Hirth, R. G. Hoagland and J. D. Embury, *Acta Mater*, 2004, **52**, 995-1002.
20. J. Wang and X. H. Zhang, *Mrs Bull*, 2016, **41**, 274-285.
21. S. Xue, Z. Fan, Y. Chen, J. Li, H. Wang and X. Zhang, *Acta Mater*, 2015, **101**, 62-70.
22. X. Zhang, A. Misra, H. Wang, M. Nastasi, J. D. Embury, T. E. Mitchell, R. G. Hoagland and J. P. Hirth, *Appl Phys Lett*, 2004, **84**, 1096-1098.
23. J. W. Wang, F. Sansoz, J. Y. Huang, Y. Liu, S. H. Sun, Z. Zhang and S. X. Mao, *Nat Commun*, 2013, **4**.
24. S. C. Xue, Z. Fan, O. B. Lawal, R. Thevamaran, Q. Li, Y. Liu, K. Y. Yu, J. Wang, E. L. Thomas, H. Y. Wang and X. H. Zhang, *Nat Commun*, 2017, **8**.
25. M. Dao, L. Lu, Y. F. Shen and S. Suresh, *Acta Mater*, 2006, **54**, 5421-5432.
26. Z. S. You, L. Lu and K. Lu, *Acta Mater*, 2011, **59**, 6927-6937.
27. E. Ma and T. Zhu, *Mater Today*, 2017, **20**, 323-331.
28. L. L. Zhu, H. H. Ruan, X. Y. Li, M. Dao, H. J. Gao and J. Lu, *Acta Mater*, 2011, **59**, 5544-5557.
29. A. Chianpairot, G. Lothongkum, C. A. Schuh and Y. Boonyongmaneerat, *Corros Sci*, 2011, **53**, 1066-1071.
30. G. Z. Meng, Y. W. Shao, T. Zhang, Y. Zhang and F. H. Wang, *Electrochim Acta*, 2008, **53**, 5923-5926.
31. G. Z. Meng, F. L. Sun, Y. W. Shao, T. Zhang, F. H. Wang, C. F. Dong and X. G. Li, *Electrochim Acta*, 2010, **55**, 2575-2581.
32. Y. Zhao, I. C. Cheng, M. E. Kassner and A. M. Hodge, *Acta Mater*, 2014, **67**, 181-188.
33. R. Mishra and R. Balasubramaniam, *Corros Sci*, 2004, **46**, 3019-3029.
34. L. G. Sun, X. Q. He and J. Lu, *Npj Comput Mater*, 2018, **4**.
35. D. C. Jang, X. Y. Li, H. J. Gao and J. R. Greer, *Nat Nanotechnol*, 2012, **7**, 594-601.
36. B. Chen, J. Wang, Q. Gao, Y. J. Chen, X. Z. Liao, C. S. Lu, H. H. Tan, Y. W. Mai, J. Zou, S. P. Ringer, H. J. Gao and C. Jagadish, *Nano Lett*, 2013, **13**, 4369-4373.
37. B. J. Wang, H. T. Zhang, J. Lou and Y. Lu, *Mater Res Lett*, 2018, **6**, 13-21.
38. C. B. C. S. I. HOLME, *PHILOSOPHICAL MAGAZINE*, 1977, **35**.
39. I. A. Ovid'ko and N. V. Skiba, *Scripta Mater*, 2014, **71**, 33-36.
40. K. Hattar, *Woodhead Publ Mater*, 2011, 213-242.
41. E. M. Bringa, A. Caro, Y. M. Wang, M. Victoria, J. M. McNaney, B. A. Remington, R. F. Smith, B. R. Torralva and H. Van Swygenhoven, *Science*, 2005, **309**, 1838-1841.
42. J. C. Villegas and L. L. Shaw, *Acta Mater*, 2009, **57**, 5782-5795.
43. D. J. Siegel, *Appl Phys Lett*, 2005, **87**.
44. J. Ding, Q. Li, J. Li, S. Xue, Z. Fan, H. Wang and X. Zhang, *Acta Mater*, 2018, **149**, 57-67.
45. J. Kacher, I. M. Robertson, M. Nowell, J. Knapp and K. Hattar, *Mat Sci Eng a-Struct*, 2011, **528**, 1628-1635.
46. K. Hattar, D. M. Follstaedt, J. A. Knapp and I. M. Robertson, *Acta Mater*, 2008, **56**, 794-801.
47. Y. F. Zhang, J. Wang, H. Q. Shan and K. J. Zhao, *Scripta Mater*, 2015, **108**, 35-39.
48. J. Li, J. Y. Zhang, G. Liu and J. Sun, *Int J Plasticity*, 2016, **85**, 172-189.
49. O. Anderoglu, A. Misra, J. Wang, R. G. Hoagland, J. P. Hirth and X. Zhang, *Int J Plasticity*, 2010, **26**, 875-886.
50. Y. Chen, K. Y. Yu, Y. Liu, S. Shao, H. Wang, M. A. Kirk, J. Wang and X. Zhang, *Nat Commun*, 2015, **6**.
51. X. Chen, W. D. Wang, S. Cheng, B. Dong and C. Y. Li, *Acs Nano*, 2013, **7**, 8251-8257.
52. H. Sun, S. H. Fu, C. C. Chen, Z. R. Wang and C. V. Singh, *Acta Mater*, 2019, **178**, 263-274.
53. J. Wang, A. Misra and J. P. Hirth, *Phys Rev B*, 2011, **83**.
54. L. Liu, J. Wang, S. K. Gong and S. X. Mao, *Phys Rev Lett*, 2011, **106**.
55. Q. Li, J. Cho, S. C. Xue, X. Sun, Y. F. Zhang, Z. X. Shang, H. Y. Wang and X. H. Zhang, *Acta Mater*, 2019, **165**, 142-152.

56. Y. F. Zhang, S. Xue, Q. Li, C. Fan, R. Su, J. Ding, H. Wang, H. Wang and X. Zhang, *Scripta Mater*, 2018, **148**, 5-9.
57. Y. Liu, D. Bufford, H. Wang, C. Sun and X. Zhang, *Acta Mater*, 2011, **59**, 1924-1933.
58. V. Torabinejad, M. Aliofkhazraei, S. Assareh, M. H. Allahyarzadeh and A. Sabour Rouhaghdam, *Journal of Alloys and Compounds*, 2017, **691**, 841-859.
59. L. Velasco and A. M. Hodge, *Mat Sci Eng a-Struct*, 2017, **687**, 93-98.
60. S. D. Dahlgren, W. L. Nicholson, M. D. Merz, W. Bollmann, J. F. Devlin and D. R. Wang, *Thin Solid Films*, 1977, **40**, 345-353.
61. L. P. Bicelli, B. Bozzini, C. Mele and L. D'Urzo, *Int J Electrochem Sc*, 2008, **3**, 356-408.
62. K. Sieradzki, S. R. Brankovic and N. Dimitrov, *Science*, 1999, **284**, 138-141.
63. A. Gomes and M. I. D. Pereira, *Electrochim Acta*, 2006, **51**, 1342-1350.
64. M. Peykova, E. Michailova, D. Stoychev and A. Milchev, *Electrochim Acta*, 1995, **40**, 2595-2601.
65. Z. P. Liu, S. Li, Y. Yang, S. Peng, Z. K. Hu and Y. T. Qian, *Adv Mater*, 2003, **15**, 1946-+.
66. R. Vittal, H. Gomathi and K. J. Kim, *Adv Colloid Interfac*, 2006, **119**, 55-68.
67. S. Xue, W. Kuo, Q. Li, Z. Fan, J. Ding, R. Su, H. Wang and X. Zhang, *Acta Mater*, 2018, **144**, 226-234.
68. R. J. Nichols, W. Beckmann, H. Meyer, N. Batina and D. M. Kolb, *J Electroanal Chem*, 1992, **330**, 381-394.
69. S. L. Thomas, A. H. King and D. J. Srolovitz, *Acta Mater*, 2016, **113**, 301-310.
70. N. Hansen, *Scripta Mater*, 2004, **51**, 801-806.
71. R. W. Armstrong, *Philosophical Magazine*, 2016, **96**, 3097-3108.
72. J. A. El-Awady, *Nat Commun*, 2015, **6**.
73. K. Lu, *Nature Reviews Materials*, 2016, **1**, 16019.
74. Q. H. Lu, Z. S. You, X. X. Huang, N. Hansen and L. Lu, *Acta Mater*, 2017, **127**, 85-97.
75. C. Fan, Q. Li, J. Ding, Z. Shang, J. Li, R. Su, J. Cho, Y. Liang, J. Wang, D. Chen, Y. Wang, H. Wang and X. Zhang, *Acta Mater*, 2019.
76. S. Xue, Q. Li, D. Y. Xie, Y. F. Zhang, H. Wang, H. Y. Wang, J. Wang and X. Zhang, *Mater Res Lett*, 2019, **7**, 33-39.
77. Q. Li, S. C. Xue, J. Wang, S. Shao, A. H. Kwong, A. Giwa, Z. Fan, Y. Liu, Z. M. Qi, J. Ding, H. Wang, J. R. Greer, H. Y. Wang and X. H. Zhang, *Adv Mater*, 2018, **30**.
78. N. Li, J. Wang, A. Misra, X. Zhang, J. Y. Huang and J. P. Hirth, *Acta Mater*, 2011, **59**, 5989-5996.
79. Z. Jin, P. Gumbsch, K. Albe, E. Ma, K. Lu, H. Gleiter and H. Hahn, *Acta Mater*, 2008, **56**, 1126-1135.
80. C. C. F. Kwan, L. Wang, K. W. Xia and Z. R. Wang, *J Mater Sci*, 2017, **52**, 13261-13270.
81. S. M. Han, M. A. Phillips and W. D. Nix, *Acta Mater*, 2009, **57**, 4473-4490.
82. M. Mieszala, G. Guillonneau, M. Hasegawa, R. Raghavan, J. M. Wheeler, S. Mischler, M. J. and L. Philippe, *Nanoscale*, 2016, **8**, 15999.
83. Z. H. Cao, Y. P. Cai, C. Sun, Y. J. Ma, M. Z. Wei, Q. Li, H. M. Lu, H. Wang, X. Zhang and X. K. Meng, *Int J Plasticity*, 2019, **113**, 145-157.
84. M. D. Uchic, D. M. Dimiduk, J. N. Florando and W. D. Nix, *Science*, 2004, **305**, 986-989.
85. J. R. Greer, W. C. Oliver and W. D. Nix, *Acta Mater*, 2005, **53**, 1821-1830.
86. A. T. Jennings, M. J. Burek and J. R. Greer, *Phys Rev Lett*, 2010, **104**.
87. A. Sharma, N. Gazit, L. Klinger and E. Rabkin, *Adv Funct Mater*, 2019, 1807554.
88. J. R. Greer, D. C. Jang, J. Y. Kim and M. J. Burek, *Adv Funct Mater*, 2009, **19**, 2880-2886.
89. X. W. Gu, C. N. Loynachan, Z. X. Wu, Y. W. Zhang, D. J. Srolovitz and J. R. Greer, *Nano Lett*, 2012, **12**, 6385-6392.
90. A. Misra, J. P. Hirth and R. G. Hoagland, *Acta Mater*, 2005, **53**, 4817-4824.
91. M. Stern and A. L. Geary, *J Electrochem Soc*, 1957, **104**, 56-63.

92. R. Rofagha, R. Langer, A. M. Elsharik, U. Erb, G. Palumbo and K. T. Aust, *Scripta Metall Mater*, 1991, **25**, 2867-2872.
93. M. Sabatini, L. Monaco and U. Erb, *Corros Sci*, 2019, doi.org/10.1016/j.corsci.2019.108233.
94. K. T. Aust, U. Erb and G. Palumbo, *Mat Sci Eng a-Struct*, 1994, **176**, 329-334.
95. M. Michiuchi, H. Kokawa, Z. J. Wang, Y. S. Sato and K. Sakai, *Acta Mater*, 2006, **54**, 5179-5184.

Figure captions

Figure 1. Fabrication and microstructure of single-crystal-like nanotwinned (nt) Ni via a hybrid technique. (a) Methodological approaches to heteroepitaxially grow nt Ni on Cu (111) coated Si substrates using either monolithic magnetron sputtering technique or a hybrid technique. (b) Crystallographic relationship between Cu (111) and Si (110) substrate. (c) An automated crystal orientation map (ACOM) of sputtered nt Ni (s-nt Ni) with coarse twin structures. The pole figure indicates textured and twinned structure. (d) ACOM of electrodeposited nt Ni (e-nt Ni) via a hybrid technique. Twin boundaries (TBs) are marked in black lines. Few ambiguities and conventional GBs are spotted and mostly all boundaries are determined as $\Sigma 3$ TBs. They exhibit wavy structure. The pole figure indicates textured and twinned structure. (e) Low-magnification Cross-sectional TEM (XTEM) micrograph showing high-density stepped nanotwins with long and irregular step morphology. (f) Corresponding SAD pattern showing a typical twin diffraction pattern. (g) Intermediate magnification TEM micrograph highlighting the stepped TBs composed of CTB and ITB segments. (h) HRTEM micrograph showing that the CTBs are decorated by kinks and stacking faults (SFs), and ITBs sometimes have diffuse character with a width of ~ 10 nm. Note: *M* and *T* stand for matrix and twin, respectively.

Figure 2. Tailoring microstructure of Ni synthesized by various conditions. (a1-a3) Sputtered nt Ni (s-nt Ni) on Cu (111) template. $\{111\}$; X-ray pole figure analysis in (a1) shows 6-fold symmetric spots arising from the matrix and twin variants. Cross-sectional focused-ion-beam ion channeling (XFIB) image in (a2) shows block-like twin structure with large twin spacing in Ni. Plan-view TEM micrograph in (a3) shows columnar grain boundaries. (b1-b3) Additive-assisted electrodeposition of nanocrystalline Ni (nc Ni) on sputtered polycrystalline Cu template. X-ray pole figure (b1) shows no sign of (111) texture in nc Ni. XFIB (b2) and plan-view TEM (b3) micrographs show the formation of nanocrystals. (c1-c3) Additive-free electrodeposition of coarse-grained (cg) Ni on sputtered nt Cu (111) template. X-ray pole figure in (c1) reveals the occurrence of twins. XFIB (c2) and plan-view TEM (c3) micrographs show inclined twin boundaries in cg Ni. (d1-d3) Additive-assisted electrodeposition of single-crystal-like nt Ni (e-nt Ni) on nt Cu (111) template. X-ray pole figure in (d1) shows the formation of high-density twins. XFIB image in (d2) displays the formation of extremely fine twins with no presence of columnar grain boundaries. Plan-view TEM image in (d3) and the inserted SAD pattern suggests single-crystal-like structure. Symbols in column I indicate the film growth direction.

Figure 3. *In situ* compression experiments (inside a scanning electron microscope) on Ni samples prepared by various processes. (a) Engineering stress-strain curves of cg Ni, nc Ni, s-nt

Ni and e-nt Ni show that e-nt Ni outperforms its counterparts. (b-e) Snapshots of deformed micropillars at different strain levels show the formation of shear off-sets in cg Ni; whereas no obvious localized deformation occurs in other samples. See supplementary movie S1-S4.

Figure 4. Post-mortem XTEM/ACOM micrographs of the single-crystal-like e-nt Ni micropillar deformed up to ~16 % strain. (a) Low magnification bright-field TEM micrograph and corresponding SAD pattern show $\{111\}$ lattice plane rotation and curved CTBs in deformed twin structures. (b) Corresponding ACOM image shows long CTBs, and the removal of irregular ITB steps in the deformed pillar top region, whereas stepped irregular twins with CTB and ITB segments remain in the lower portion of less deformed region. The pole figure indicates lattice plane rotation. (c) TEM image shows curved TBs after deformation, and the rotation of (111) planes in matrix and twins. (d) TEM image shows the formation of steps along CTBs and the dislocation activities. Abundant Frank partials form adjacent to CTBs. (e) High-resolution TEM image shows 90° Shockley partials are blocked by TBs containing SFs and steps.

Figure 5. Potentiodynamic polarization curves of bulk-cg Ni, nc Ni, s-nt Ni and e-nt Ni in artificial seawater. The e-nt Ni shows most positive corrosion potential and lowest correction current density amongst various Ni specimens.